



Experiment Report Form

The double page inside this form is to be filled in by all users or groups of users who have had access to beam time for measurements at the ESRF.

Once completed, the report should be submitted electronically to the User Office via the User Portal:
<https://www.esrf.fr/misapps/SMISWebClient/protected/welcome.do>

Deadlines for submission of Experimental Reports

Experimental reports must be submitted within the period of 3 months after the end of the experiment.

Experiment Report supporting a new proposal (“relevant report”)

If you are submitting a proposal for a new project, or to continue a project for which you have previously been allocated beam time, you must submit a report on each of your previous measurement(s):

- even on those carried out close to the proposal submission deadline (it can be a “*preliminary report*”),
- even for experiments whose scientific area is different from the scientific area of the new proposal,
- carried out on CRG beamlines.

You must then register the report(s) as “relevant report(s)” in the new application form for beam time.

Deadlines for submitting a report supporting a new proposal

- 1st March Proposal Round - **5th March**
- 10th September Proposal Round - **13th September**

The Review Committees reserve the right to reject new proposals from groups who have not reported on the use of beam time allocated previously.

Reports on experiments relating to long term projects

Proposers awarded beam time for a long term project are required to submit an interim report at the end of each year, irrespective of the number of shifts of beam time they have used.

Published papers

All users must give proper credit to ESRF staff members and proper mention to ESRF facilities which were essential for the results described in any ensuing publication. Further, they are obliged to send to the Joint ESRF/ ILL library the complete reference and the abstract of all papers appearing in print, and resulting from the use of the ESRF.

Should you wish to make more general comments on the experiment, please note them on the User Evaluation Form, and send both the Report and the Evaluation Form to the User Office.

Instructions for preparing your Report

- fill in a separate form for each project or series of measurements.
- type your report in English.
- include the experiment number to which the report refers.
- make sure that the text, tables and figures fit into the space available.
- if your work is published or is in press, you may prefer to paste in the abstract, and add full reference details. If the abstract is in a language other than English, please include an English translation.



	Experiment title: Imaging the magnetisation vector field by Fourier Transform Holography	Experiment number: MI-1384
Beamline: ID32	Date of experiment: from: June 22 nd 2021 to: June 28 nd 2021	Date of report:
Shifts: 18	Local contact(s): Flora Yakhou-Harris	<i>Received at ESRF:</i>
Names and affiliations of applicants (* indicates experimentalists): *Guillaume Beutier, SIMaP Feodor Ogrin, University of Exeter Gerrit Van der Laan, Diamond Light Source Farid Fettar, Institut Néel Marc Verdier, SIMaP *Marisel Di Pietro-Martinez, SIMaP *Carlos Herrero Martinez, SIMaP *Alexis Wartelle, SIMaP		

Report:

Objectives

The present proposal aimed at unlocking the capability of X-ray-based Fourier Transform Holography (FTH) to image not only the scalar transmission of an object [1] but also vector fields, in this case magnetization within a finite-sized object.

For this study, the contrast mechanism was X-ray Magnetic Circular Dichroism (XMCD), which has been used with FTH for almost two decades already. While the first report of XMCD-FTH focused on the imaging of magnetic worm-like domains perpendicular to the sample substrate [2], the method was then extended to measure in-plane magnetization components [3,4]. In the latter work, use was made of the so-called HERALDO method: Holography with Extended Reference Autocorrelation Linear Differential Operator [5]. With HERALDO, pinpoint references are no longer necessary and more readily prepared shapes such as slits become relevant. In that case, proper filtering in reciprocal space allows to suppress the effect of the slit except for its tips, which then act as point references [5]. Not only does this ease the Focused Ion Beam (FIB) milling of references, it also allows significant X-ray flux through the reference when the sample is tilted with respect to normal incidence [4]. In this geometry, XMCD provides a sensitivity to in-plane magnetization along the slit. So far, XMCD-based imaging of the two in-plane components of magnetization has been realized with full field Magnetic Transmission X-ray Microscopy (MTXM) [6], PhotoEmission Electron Microscopy (XMCD-PEEM) [7], Small-Angle X-ray Scattering utilizing ptychography [8] or Scanning Transmission X-ray Microscopy (STXM) used in a laminography geometry [9]. Yet, no reports of magnetic vector FTH experiments exist to date.

Contrary to the aforementioned methods, FTH possesses the strong advantage of being self-referenced i.e. it is by nature mostly insensitive to sample drifts. With HERALDO, strong magnetic contrast at large incidence angles becomes accessible, thus allowing vector magnetic FTH by combining two orthogonal reference slits. Building on experience acquired at synchrotron SOLEIL, we fabricate isolated, finite-sized objects out of magnetic materials on one side of a thin Si₃N₄ membrane. A thick Au film is deposited on the other side of the silicon nitride window, then etched away with FIB to (i) define an aperture centered around the object of interest, and (ii) define two orthogonal extended reference slits, which correspond to traversing holes through the hole sample.

Sample Fabrication

Fe/Gd multilayers

Beutier17

The first sample we imaged on ID32 was an Fe/Gd multilayer which also had been imaged at SOLEIL (SEXTANTS beamline). The stacking for this sample is as follows:



This leads to an average composition Fe_{0.568}Gd_{0.432}. The total stack's thickness as determined from Scanning Electron Microscopy (SEM) measurements is about 800 nm. In terms of lithography, only FIB was performed to create an aperture in the gold (on the backside) to define a finite-size disk object, as well as two orthogonal slits traversing the whole sample. The following two images show the feature that was imaged, after milling, from the side of the magnetic multilayer (left) and from the side of the thick gold layer (right), focusing on one of the slits.

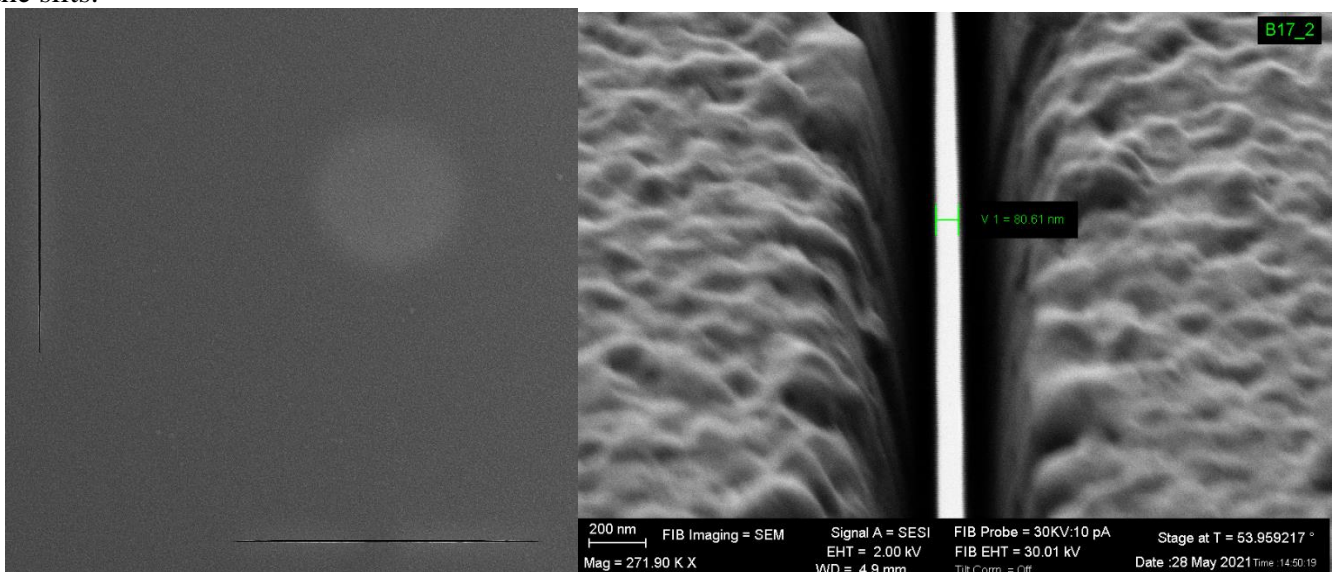


Fig. 1: SEM images of sample Beutier17 after FIB patterning. Left: image taken from the side of the magnetic multilayer; the object appears as a brighter disk. Right: image acquired from the side of the thick Au layer, focusing on one of the reference slits.

Dann112

Dann112 is another Fe/Gd multilayer with the following stacking:



The total thickness is about 80 nm. This sample is similar to Beutier17 in terms of design: all four fabricated devices also feature two orthogonal slits and an aperture in its gold layer of about 5 μm in diameter to define an object. However, contrary to Beutier17, this sample's magnetic multilayer was further milled (inside the field of view defined by the apertures) into isolated disks in every device. The goal was to image an object that is

fully contained inside the aperture instead of extending further: this situation (applying to Beutier17) leads to the presence of broad imaged regions that do not overlap for large differences of incidence angle. To put it differently: the actual field of view on the silicon nitride membrane changes with the incidence angle, and due to the thickness of the gold layer and the resulting shadowing, the larger the incidence angle, the further away from the aperture's center does the field of view's center lie.

In order to overcome such issues, Dann12 was milled into disks of ca. $2.5\ \mu\text{m}$ diameter. The following SEM image shows the disk that was imaged during this beamtime. The hole at its center traverses the whole sample, and was milled for the sake of aligning the multilayer's disk with respect to the gold aperture on the other side. Finally, the opening around the disk was created with a diameter of about $10\ \mu\text{m}$ to make sure it would be larger than the $5\ \mu\text{m}$ aperture in gold (on the other side).

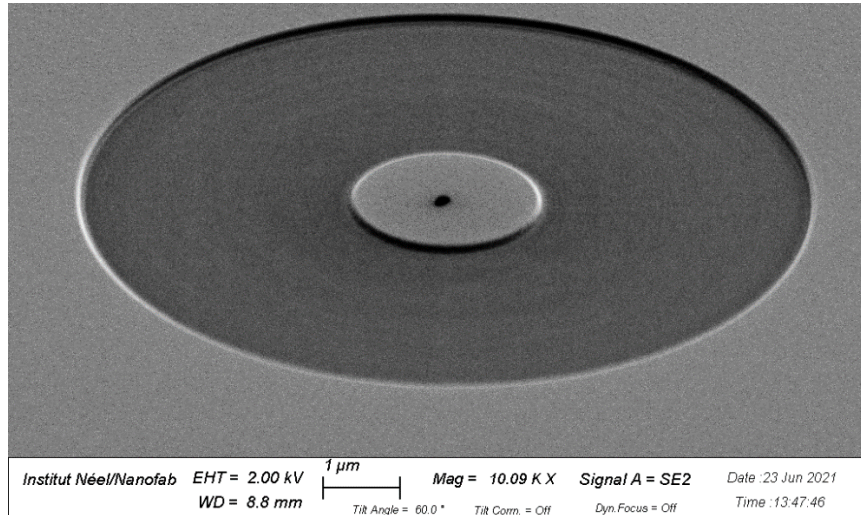


Fig. 2: SEM image of sample Dann12 after FIB patterning, viewed from the side of the magnetic multilayer. The dark dot in the center is a hole through the whole sample for purposes of aligning the disk object with the aperture in the thick gold layer.

On the next SEM images, the same structure is imaged from the side of the gold layer. The first image shows an overview, the two others focus on the aperture in gold and on the ends of the tips that were used for imaging. The spots on the second image consist of gold remaining after the etching; in addition, one can see the traversing hole etched in the center. The third image highlights the differences in slit shape resulting from two distinct milling strategies. The first one (top slit) with a “spoon-like” resulting shape aims at obtaining the narrowest possible slits but due to constraints in the motion of the ion beam as well as redeposition of material, the slit width is not homogeneous. Moreover, the width very close to the tip (ca. $80\ \text{nm}$) is very similar to the one obtained with the second strategy (bottom slit) which prioritizes a homogeneous width.

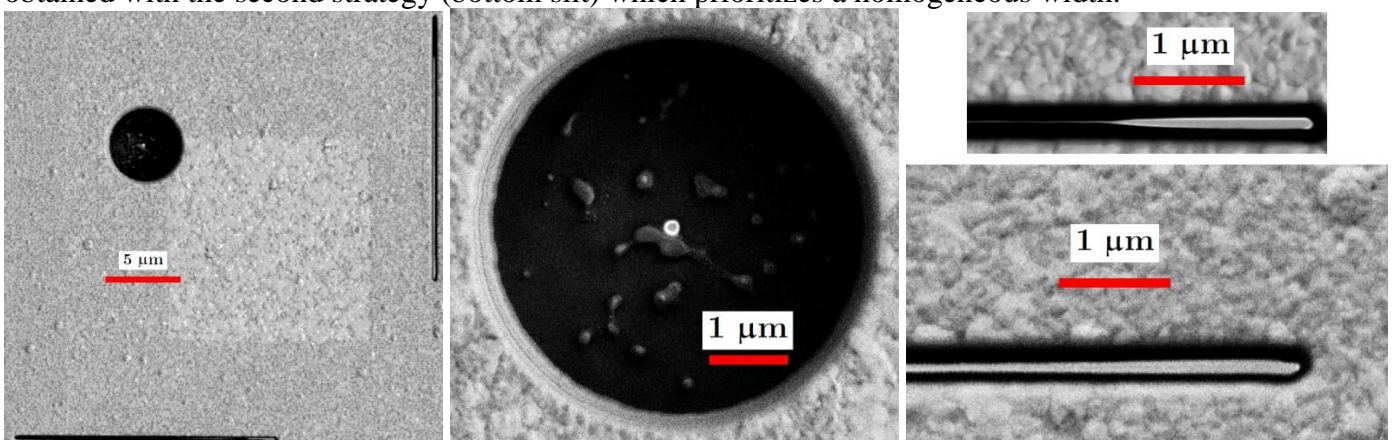


Fig. 3: SEM images of sample Dann12 from the side of the Au layer. Left: overview; middle: details of the object-defining aperture with Au residues (brighter) on the Si_3N_4 membrane (darker); right: details of the tips of the reference slits used in this experiment.

NiFe teardrop

The teardrops were fabricated using electron beam lithography, followed by a deposition of a 80-nm-thick permalloy ($\text{Ni}_{80}\text{Fe}_{20}$) layer, then lift-off.

Experimental set-up

The experiment was performed on ID32 in the usual chamber dedicated to FTH. We used the Fe L_3 edge and Gd M_5 edge to obtain magnetic contrast from our samples. The coherence of the beam was ensured by two pinholes of: the first one (100 μm in diameter) 3.56 m upstream the sample, and the second one (50 μm in diameter) 20 cm before the sample. In order to have access to the 3 components of the magnetization vector field, the beamline staff implemented a new azimuthal rotation supported by the existing tilt rotation. The azimuthal rotation, which fits in the 15 mm wide gap between the poles of the in situ electromagnet, allows rotating the azimuth by 90° , hence converting the tilt angle from one transverse axis to the perpendicular transverse axis. Because of the geometry of the azimuthal rotation, the tilt angle was restricted to $\pm 45^\circ$.

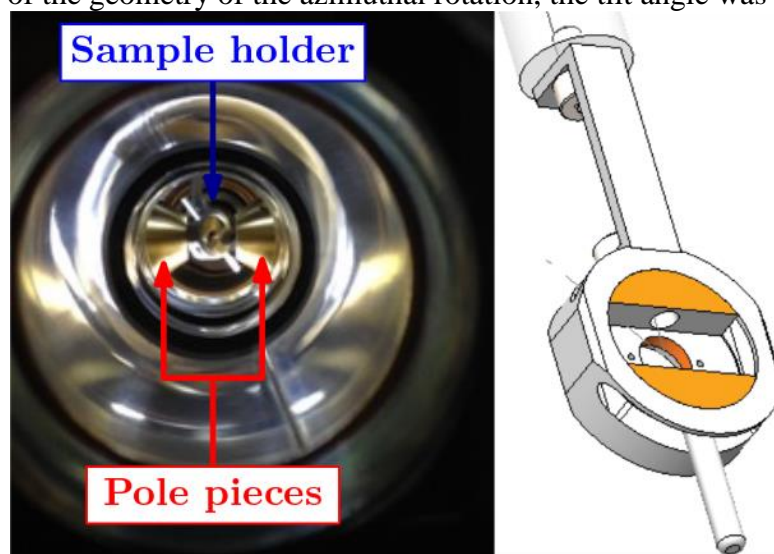


Fig. 4: Photograph of the sample holder at maximum tilt inside the electromagnet's gap (left) and detailed CAD view of the sample holder (right). The tilt axis is along the rod, and the handle (at the bottom) allows to switch between the two available azimuths.

A new detector, an in-vacuum integration of a sCMOS camera "Dhyana95" from Tucsen (commercialized by Axis Photonique) with pixel size 11 μm , fully prototyped and tested at SOLEIL, was set-up in replacement of the old CCD camera. While this new detector could in principle tremendously speed up data acquisition [10], we faced severe issues with the control software, which instead degraded a large part of the acquisitions (more details will be given in the conclusion). Furthermore, some issues with the temperature control resulted in slow accumulations of matter (presumably water) on the camera chip over the course of the beamtime.

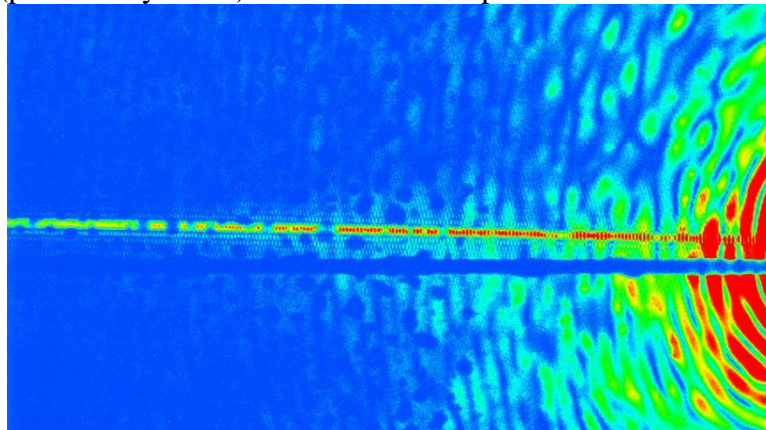


Fig. 5: Stains (see notably along the horizontal diffraction streak) on the camera noted towards the end of the beamtime.

Experimental results

Beutier17

Fe L₃ edge imaging and comparison between ID32 and SEXTANTS (Soleil)

Below are two images for comparison; the left-hand side one was taken at SOLEIL, the right-hand side one on ID32, both were acquired at the Fe L₃ edge:

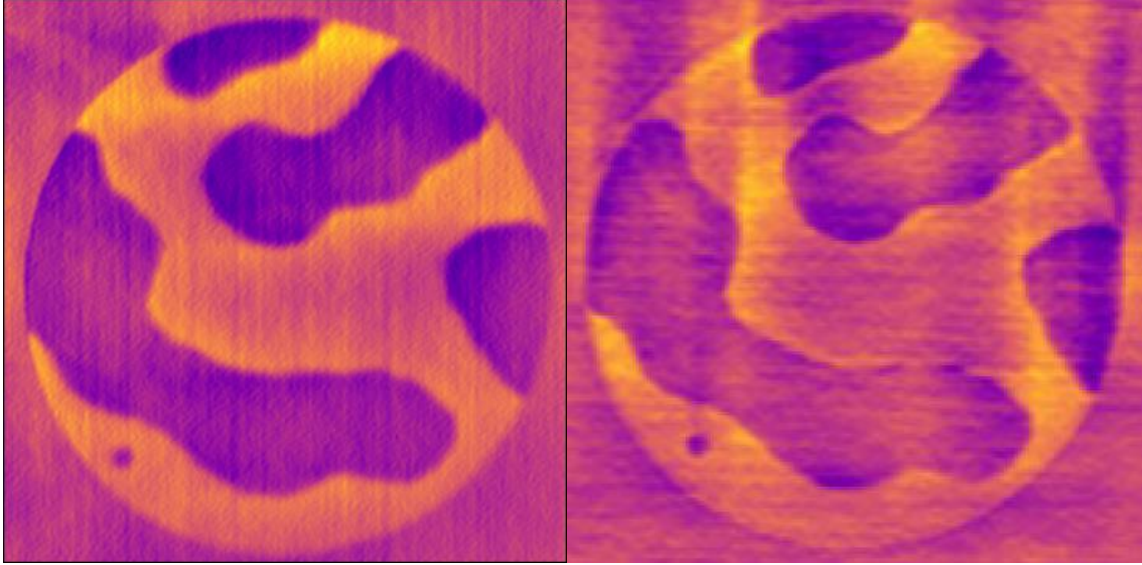


Fig. 6: Projections of magnetization perpendicular to the sample obtained with FTH on sample Beutier17, at the Fe L₃ edge. Left: image obtained on the SEXTANTS beamline at SOLEIL. Right: image acquired on ID32.

The levels of signal-to-noise ratio are quite comparable; it must be noted that the colour scales are adjusted to the images' extremal contrast values. However, on the image recorded on ID32, the contrast levels seem less well-defined over a domain than they are on the left-hand side image. One possible explanation is the different size of beam stop used on ID32 with respect to the SEXTANTS beamline at SOLEIL. Indeed, the size of the beam stop on ID32 normalized by the typical speckle radial width (estimated as a diffraction ring's full width) is larger than the same quantity evaluated from scattering patterns obtained at SEXTANTS. We find:

$$\left. \frac{W_{beamstop}}{W_{speckle}} \right|_{ID32} \approx 7.2 \pm 1.2$$
$$\left. \frac{W_{beamstop}}{W_{speckle}} \right|_{SEXTANTS} \approx 4.6 \pm 0.5$$

As a result, even for an optimal beam stop positioning, more information at low wavenumbers is cut out on ID32; we think that this results in a high-pass filtering that is more pronounced than on SEXTANTS, and which explains the aforementioned difference.

Imaging at the Gd M₅ edge

With the benefice of hindsight and Fe L₃ edge absorption spectra acquired on SEXTANTS, we realized that FTH should be possible at the Gd M₅ edge. At SOLEIL, we failed to perform imaging of sample Beutier17 at photon energies around the nominal value of the M₅ peak; no speckle was visible on scattering patterns. We now understand this as a consequence of sample thickness: the amount of material traversed by X-rays is so large that the transmitted light becomes dominated by light other than the beam of interest [11].

One solution consists in working further below the edge peak than what is usually done, in order to retrieve an X-ray absorption low enough to allow appreciable scattering. We did this on SEXTANTS, as illustrated by the following figure:

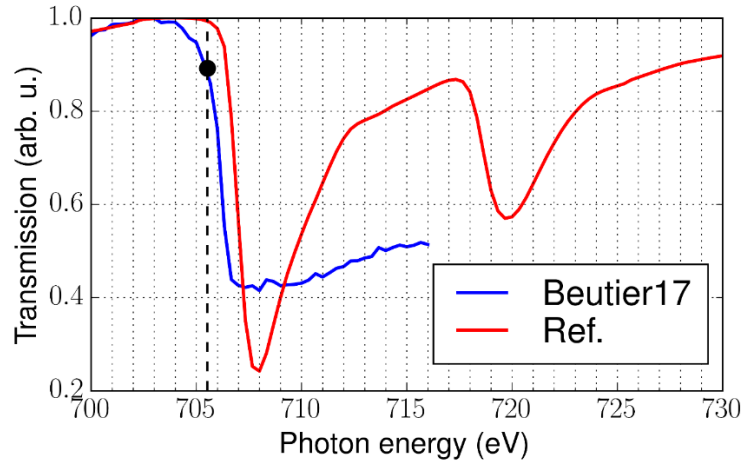


Fig. 7: Absorption spectra measured through sample Beutier17 (blue curve) and through a thin, pure Fe film labelled “Ref.” (red curve).

This represents two transmission measurements: one through a beamline filter out of pure Fe, labelled as “Ref.”, the other one through sample Beutier17. The black dot indicates the energy at which the FTH was performed at Soleil. It can be clearly seen that this found optimum lies well below the inflexion peak on the absorption edge, which is commonly the energy chosen for such measurements.

On ID32, we found the peak of the Gd M_5 edge at about 1189 eV, close to its nominal position. However, we found optimal contrast at photon energies around 1184 eV (and some non-vanishing contrast at 1180 eV still); the following figure displays the result of a reconstruction at this energy (right-hand side) and a reconstruction at the Fe L_3 at SOLEIL (left-hand side):

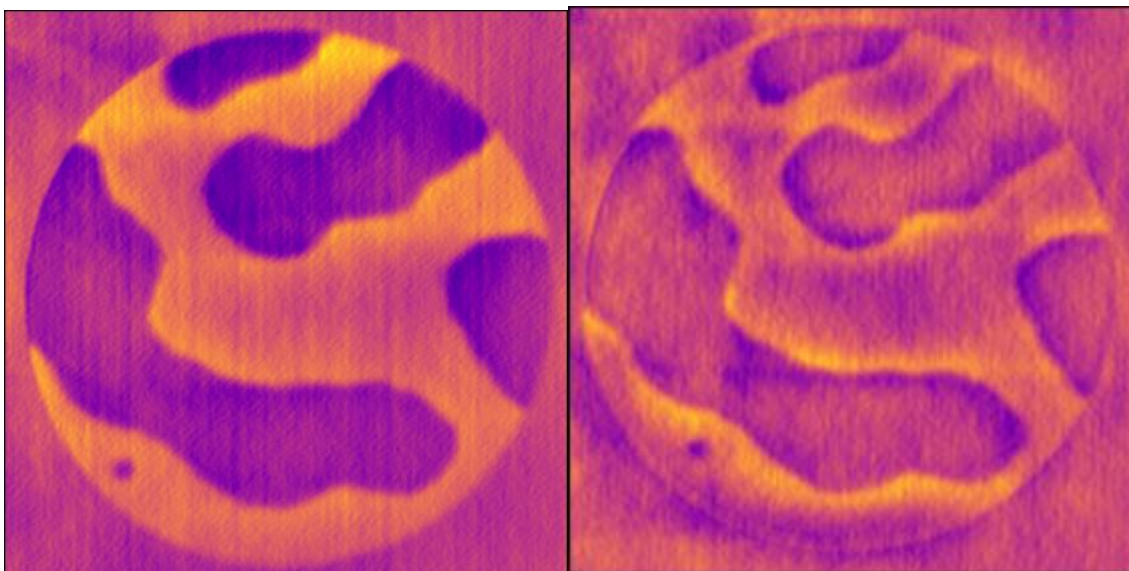


Fig. 8: Projections of magnetization perpendicular to the sample obtained with FTH on sample Beutier17, at the Fe L_3 edge on SEXTANTS (left) and on ID32 at the Gd M_5 edge (right) respectively.

The same pattern as above can easily be recognized. We ascribe most of the differences to an unwanted high-pass filtering of our scattering data due to the beam stop. As discussed above, the latter is larger (compared to the typical speckle size) than it is on SEXTANTS, and this only becomes more pronounced at higher photon energy. To further illustrate this effect, the following figure shows scattering patterns recorded (on ID32) on Beutier17 at the Gd M_5 edge (left) and at the Fe L_3 edge (right).

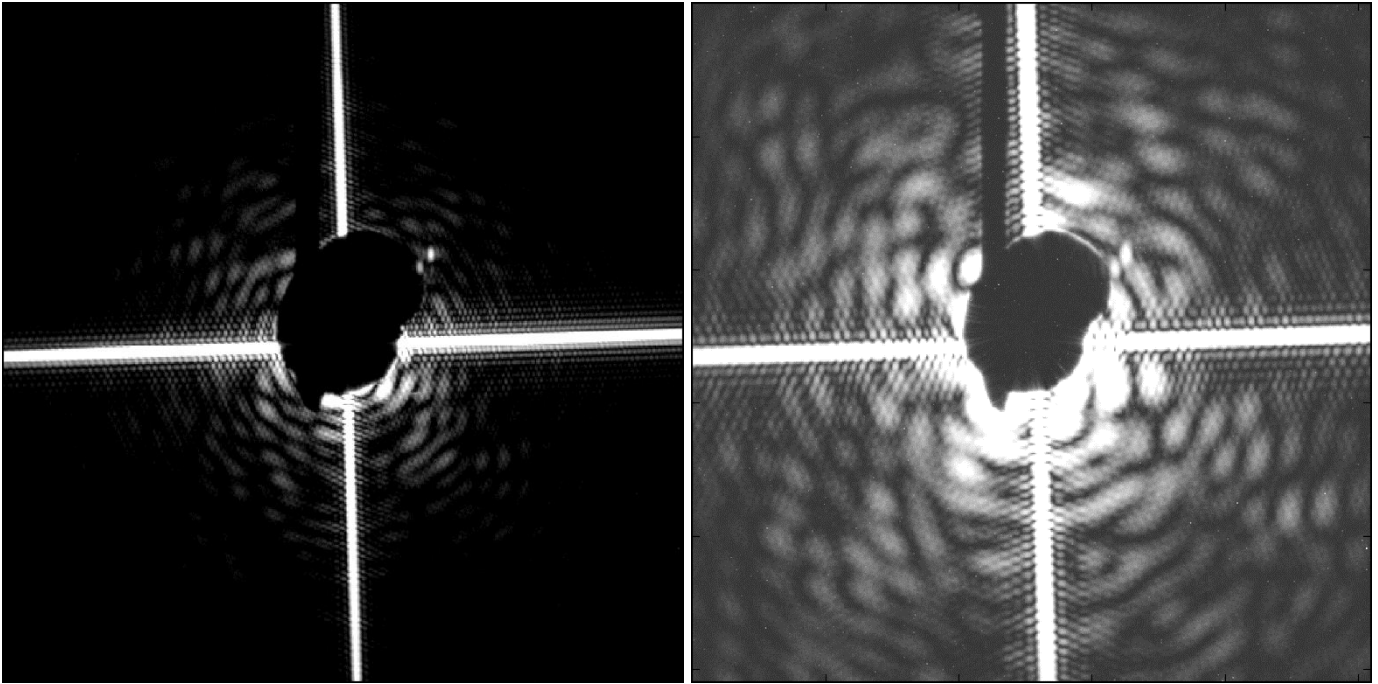


Fig. 9: Scattering patterns from sample Beutier17 obtained on ID32 at the Gd M_5 edge (left) and the Fe L_3 edge (right), respectively.

Both patterns are represented in logarithmic scale, with an identical dynamic range with respect to the image's maximum. The comparison does convey the fact that at the Gd M_5 edge, much of the central speckle is cut out, leading to a high-pass filter acting on our data; this is consistent with the rather sharp magnetic domain walls and aperture sboundary seen previously on one hand, and with the slowly-varying contrast across uniform domains on the other hand.

As for the two bright dots on the top-right side of the beam stop, we attribute them to the presence of another aperture object as well as a fully traversing hole through the sample in the vicinity of the imaged aperture. The dots are most likely stray light scattered from these two features on sample Beutier 17.

Conclusion

Although only little time was dedicated to measurements on Beutier17, several interesting elements of comparison with SEXTANTS as well as prospects regarding the development of ID32 can be drawn:

- a quality of FTH images similar to that of SEXTANTS can be reached on ID32, in spite of the ESRF's being a synchrotron specialized for hard X-rays,
- thick magnetic systems actually can be imaged provided the proper energy is found; moreover, we think our XMCD-FTH imaging at the Gd M_5 edge on ID32 to be the first of its kind,
- comparing the latter data with imaging done at the Fe L_3 edge, we are able to identify the beam stop as a beamline element where improvements (in terms of size and shape) could clearly benefit the measurements.

NiFe teardrop

The teardrop sample was briefly imaged on ID32 with the goal to confirm and if possible understand the images taken on SEXTANTS. There, only weak magnetic contrast was observed, and instead of the broad flux-closure pattern expected for such a permalloy ($Ni_{80}Fe_{20}$) element, a large number of small domains were observed. In order to have a reference, the following figure presents an image of that sample taken at SOLEIL, at the Fe L_3 edge:

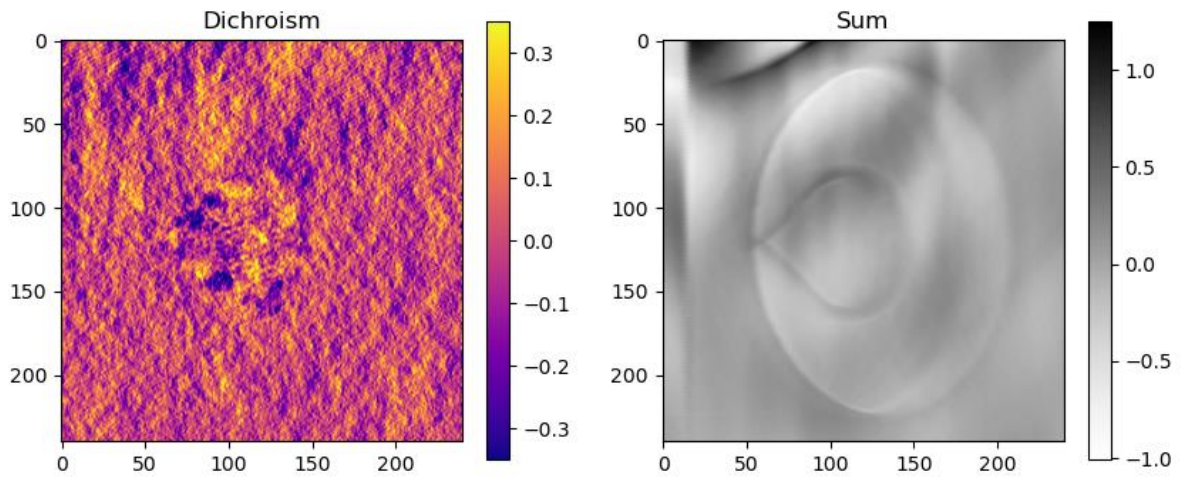


Fig. 10: Magnetic (left) and structural (right) images of the teardrop sample obtained at the Fe L_3 edge on the SEXTANTS beamline.

The left-hand side image is the dichroic contrast, the right-hand side is the charge reconstruction. The X-ray incidence angle is about 37° (away from normal incidence). Quite clearly, the signal-to-noise ratio on the magnetic part is very weak.

We could obtain a similar image on ID32 for an incidence angle of 40° , as shown below.

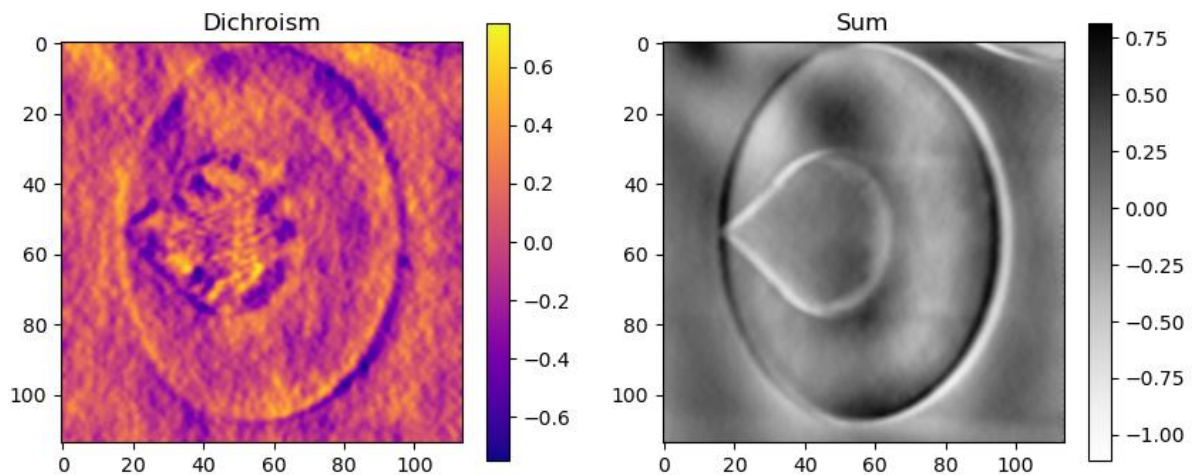


Fig. 11: Magnetic (left) and structural (right) images of the teardrop sample obtained at the Fe L_3 edge on ID32.

Interestingly, the signal-to-noise ratio seems slightly better. We can identify at least a few common features in the dichroic images; notably, the bright crescent roughly in the middle of the teardrop. However, these are far from the expected pattern, which is schematically represented on the following figure.

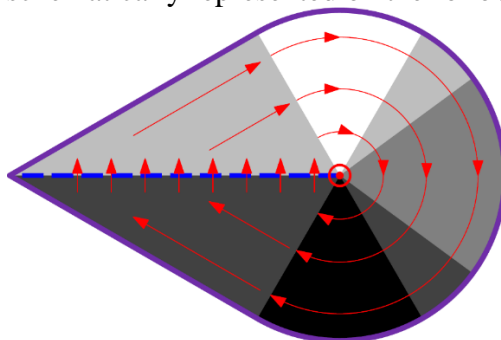


Fig. 12: Schematic representation of the expected domain pattern in the teardrop sample.

Here, magnetization is displayed as red arrows, the XMCD contrast as grey patches, and the blue dashed line corresponds to the domain wall which should form along the wedge's bisector.

In order to try and obtain this pattern, we applied a magnetic field of about 0.45 T, with an angle between the field and the normal to the sample of 75° . In other words, the field was mostly in-plane with a 0.43 T component, and that component was aligned with the bisector of the teardrop's wedge. By contrast with the SEXTANTS beamline, where only much weaker fields can be produced in FTH (~ 20 mT), the availability of such strong fields on ID32 is a great asset for XMCD-FTH experiments.

However, we obtained the following image after application of field:

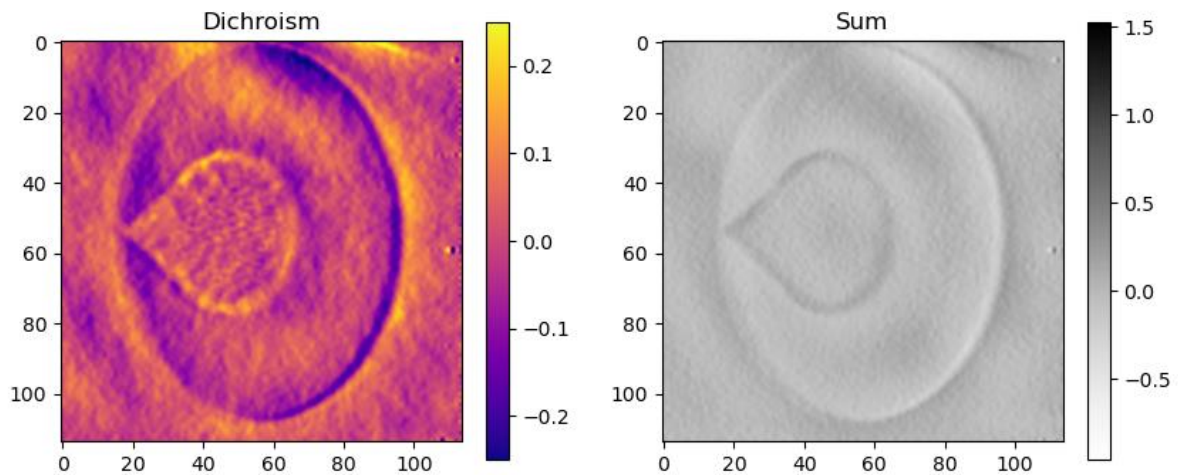


Fig. 13: Magnetic (left) and structural (right) images of the teardrop sample obtained at the Fe L_3 edge on ID32 after application of field.

Unfortunately, we could not obtain any clearer dichroic contrast than in the above image. Considering the weakness of the magnetic signal, we chose to change sample. After the beamtime, we found that this image acquisition was particularly disturbed by issues with the camera's temperature regulation.

Dann112

The different devices under normal incidence

Before focusing on the one disk that has been mostly imaged during this beamtime, we acquired images of all four devices that had been fabricated on Dann 112 with the X-ray beam perpendicular to the sample. Here is the image obtained on the first device or "zone":

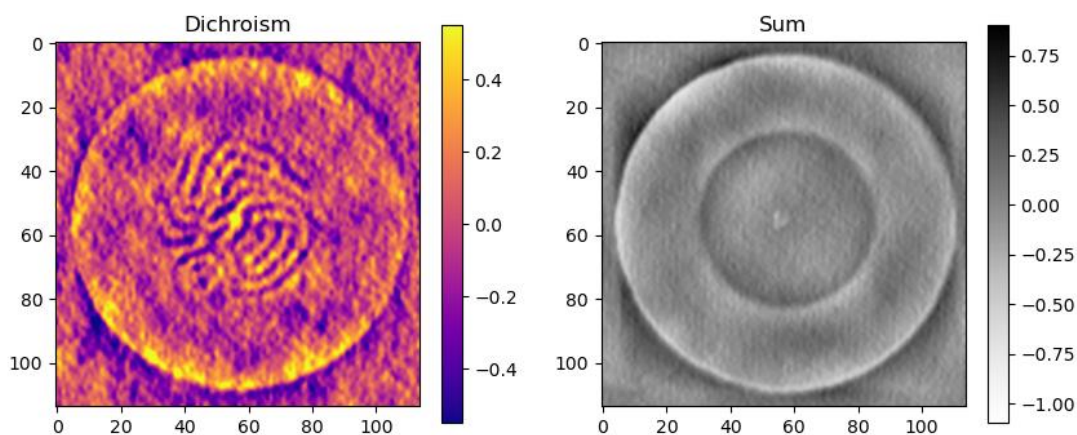


Fig. 14: Magnetic (left) and structural (right) images of the first (out of four) devices patterned into sample Dann112. Both were obtained at the Fe L_3 edge.

As a way to confirm that both slits can be used in this configuration, we checked e.g. on the 2nd zone that images can be obtained from one or the other independently, as shown below:

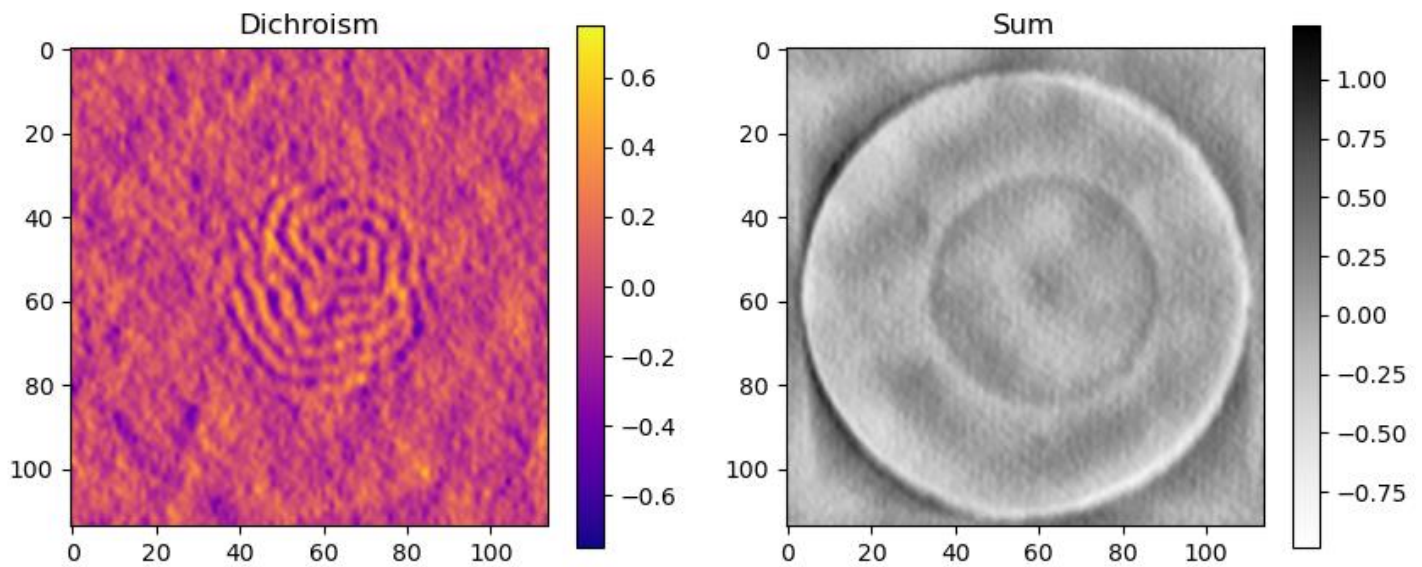


Fig. 15: Magnetic (left) and structural (right) images of the second device patterned into sample Dann112. Both were obtained at the Fe L_3 edge, using this device's vertical slit.

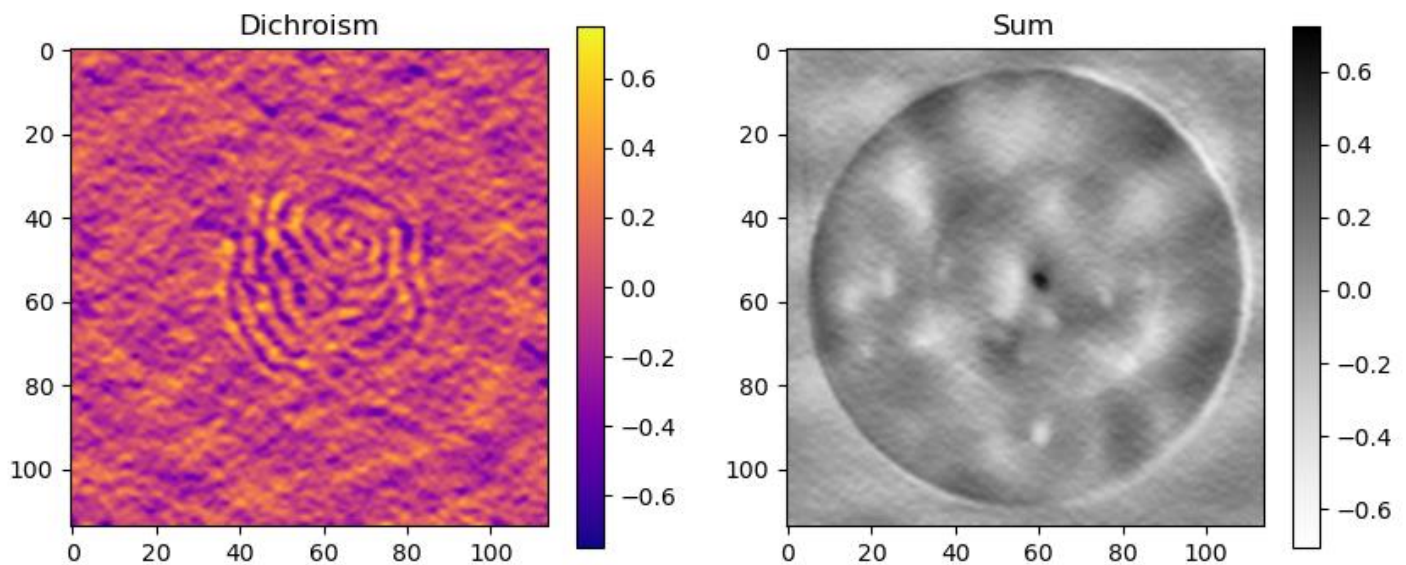


Fig. 16: Magnetic (left) and structural (right) images of the second device patterned into sample Dann112. Both were obtained at the Fe L_3 edge, using this device's horizontal slit.

The 3rd zone did not show any clear dichroic contrast. The 4th one, on which we performed almost all of our imaging in this beamtime, did display a promising dichroic pattern. The following two images correspond to the two orthogonal slits again. We point out that there is a replica of our object in the reconstruction (most visible on the charge image, to the left); it is a consequence of the "spoon-like" shape of one of the slits, cf. the sample fabrication subsection about Dann112. The part where it becomes thinner acts as a secondary tip due to the filter we apply in reciprocal space.

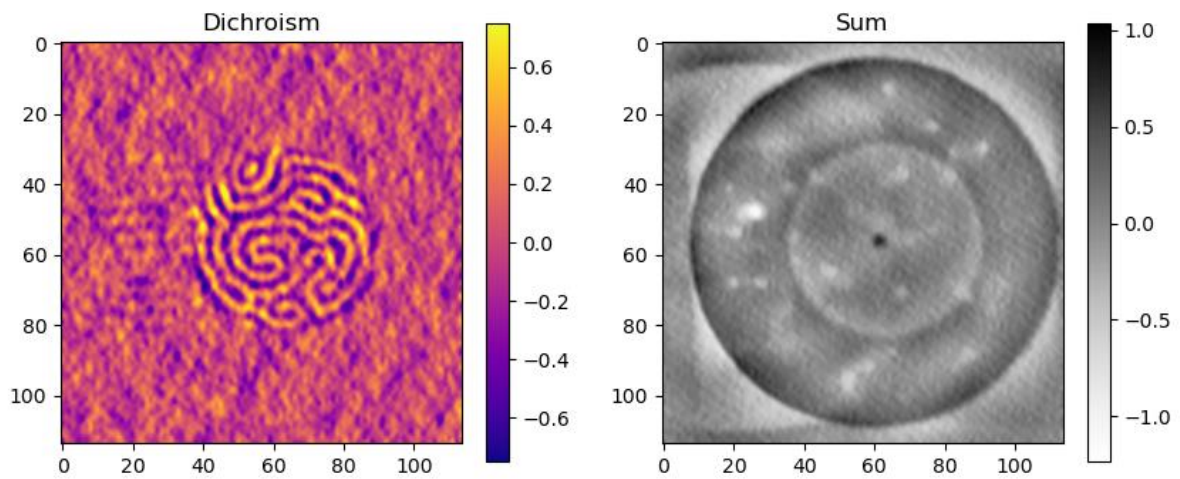


Fig. 17: Magnetic (left) and structural (right) images of the fourth device patterned into sample Dann112. Both were obtained at the Fe L_3 edge, using this device's horizontal slit.

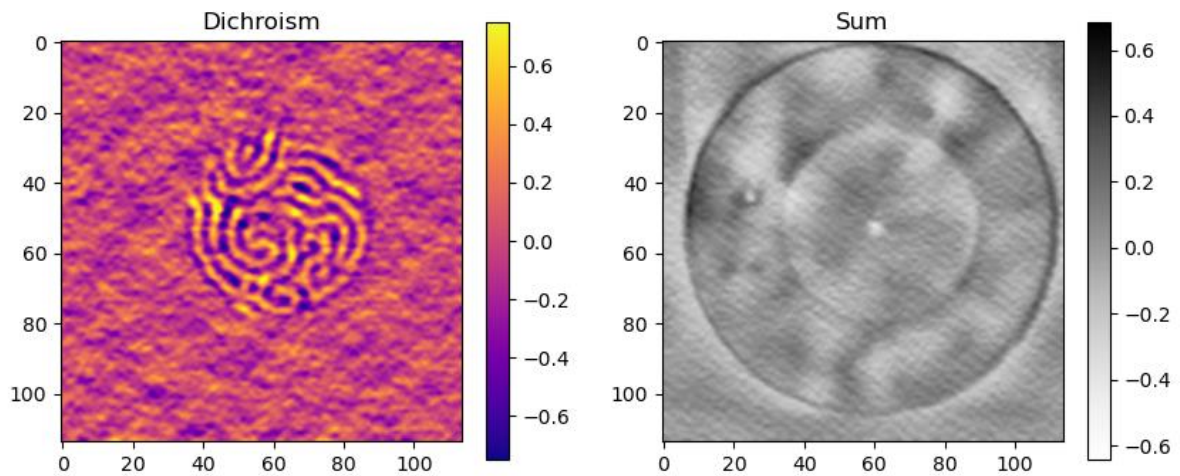


Fig. 18: Magnetic (left) and structural (right) images of the fourth device patterned into sample Dann112. Both were obtained at the Fe L_3 edge, using this device's vertical slit.

One can see very clear worm-type domains as well as isolated, bubble-like domains. It must be noted that the white dots on the top "Sum" image are no artefacts: they correspond to the gold remaining after the FIB milling that defines the aperture on one side of the membranes. Below is shown a comparison between the FTH and SEM images:

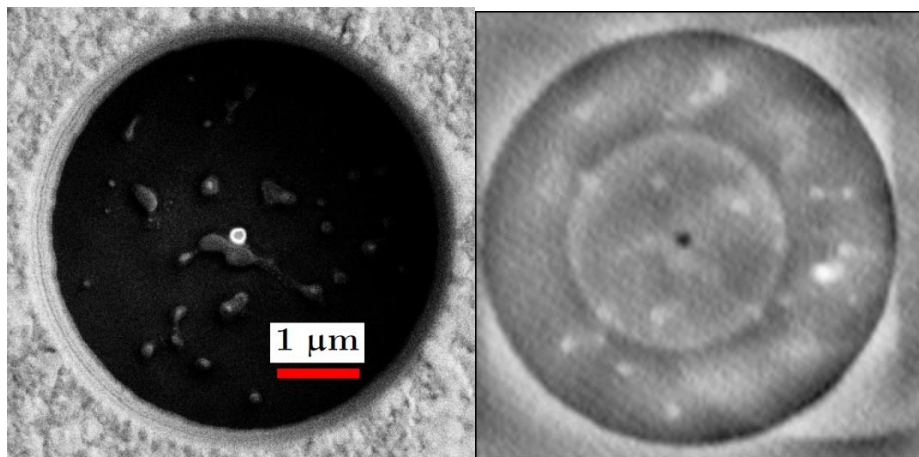


Fig. 19: SEM image of the fourth device on Dann112 from the Au layer's side (left) and corresponding FTH structural image (right), displaying even the Au residues visible on the SEM image.

Many features appear common to both images, testifying to the quality of our reconstructions.

Tilted imaging of zone 4

We first show an image taken with 20° incidence. Despite the not so great statistics, one can still recognize some specific domains seen in normal incidence.

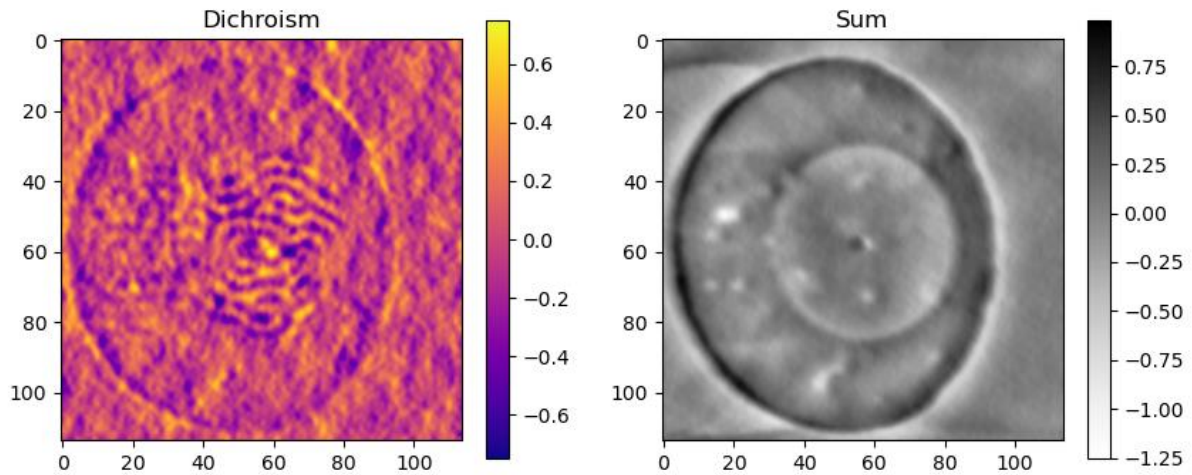


Fig. 20: Magnetic (left) and structural (right) images of the fourth device patterned into sample Dann112 at 20° degree tilt.

The following image was acquired at -35° degree incidence, or equivalently 35° degree incidence and an azimuth rotated by 180° .

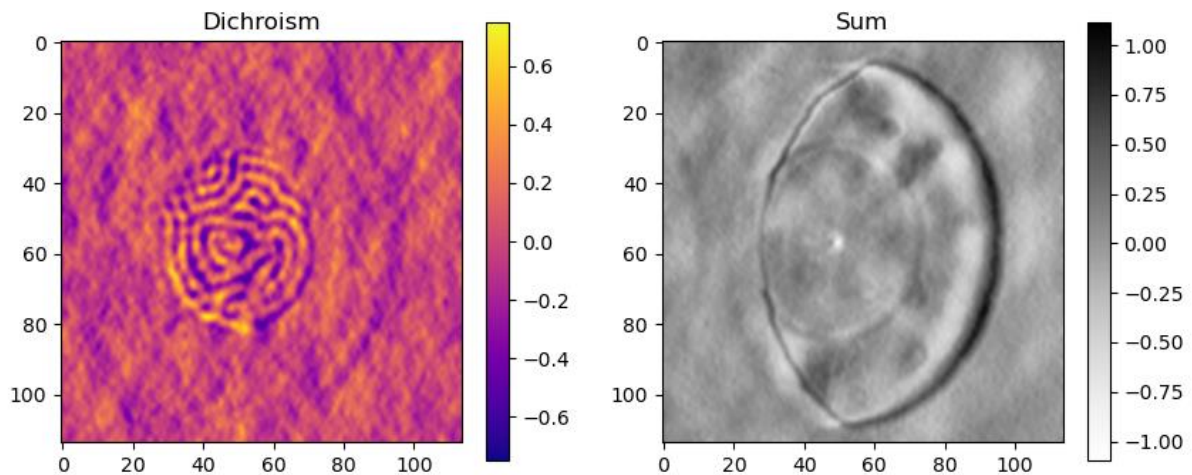


Fig. 21: Magnetic (left) and structural (right) images of the fourth device patterned into sample Dann112 at -35° degree tilt.

Since our goal is to demonstrate vector magnetic FTH, we also performed imaging after rotating the sample's azimuth by 90° so as to use the other slit on this device and therefore gain sensitivity to the second in-plane component of magnetization.

Tilted imaging of zone 4 with an azimuth rotated by 90°

Here, we show two examples of imaging performed after rotating the sample's azimuth by 90° . The first image is taken with an X-ray incidence of -45° , the second one with $+30^\circ$.

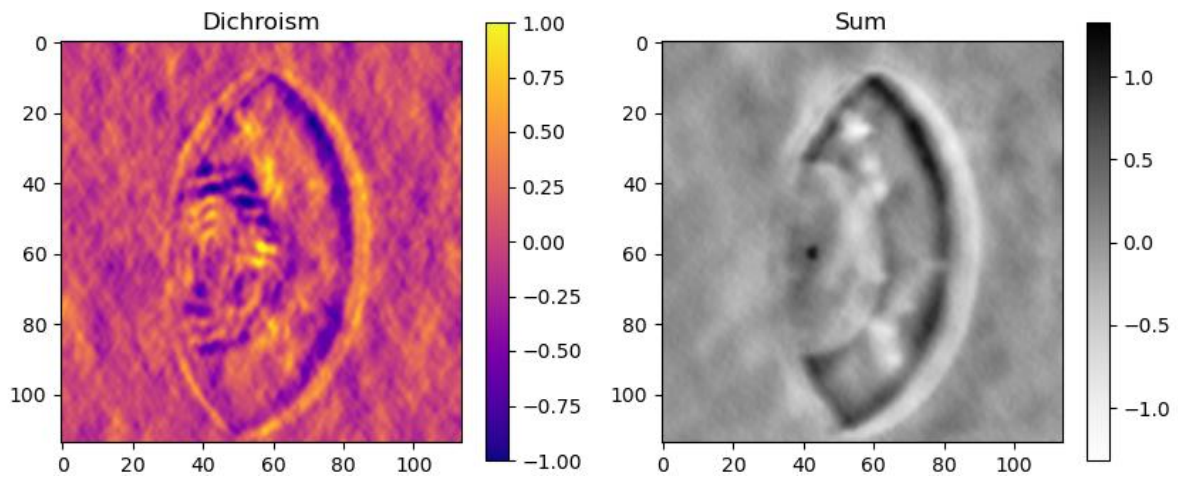


Fig. 22: Magnetic (left) and structural (right) images of the fourth device patterned into sample Dann112 at -45 degree tilt, with the second available azimuth (at 90 degree).

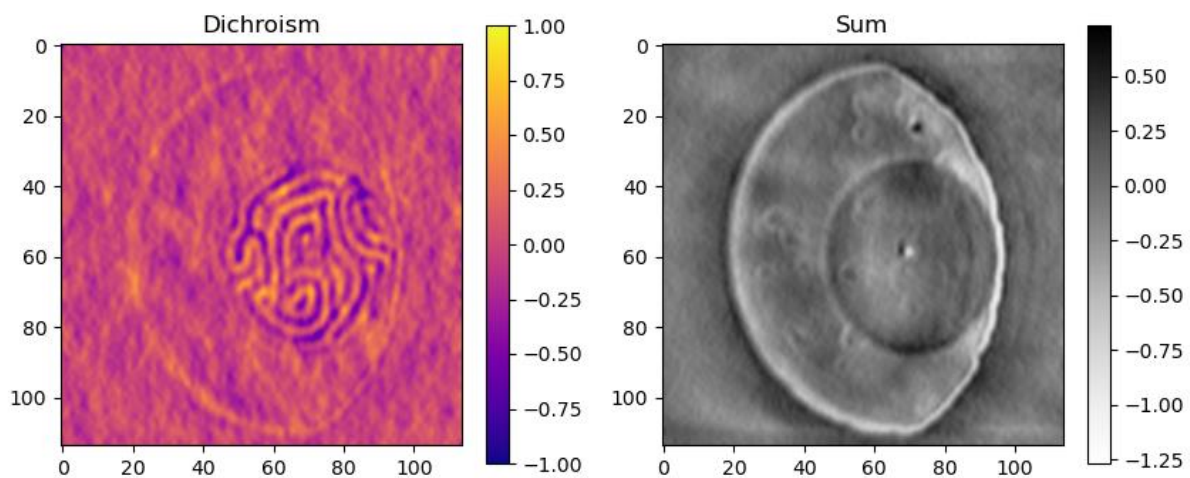


Fig. 23: Magnetic (left) and structural (right) images of the fourth device patterned into sample Dann112 at +30 degree tilt, with the second available azimuth (at 90 degree).

The final steps of our post-processing will be an attempt at combining our series of images (not all are shown here for the sake of clarity) and reconstructing the domain configuration in this Fe/Gd patterned multilayer. Currently, we are still post-processing the data to that end.

Conclusion

First of all, it must be noted that this beamtime has been significantly hampered by several kinds of camera issues. This is because its control under SPEC and under beam could not be tested before the beamtime. Overall, a combination of SPEC-related bugs and a camera operation still in the discovering led to a very unreliable image acquisition. A very large number of scans were interrupted because the camera stalled for reasons which are not yet fully understood. Moreover, we have found out that in certain cases the camera's temperature regulation aims at temperatures different from the user-defined target until a new scan is started. Even after investigation by the beamline staff the reasons for this behaviour is not known. However, the consequence is that whenever this happens, the image quality decreases and degrades an entire scan. Finally, there have been gradual accumulations of matter on the detector chip, which of course deteriorate the image quality.

This being said, already a significant number of control issues have been solved by the beamline staff and the remaining ones are going to be taken care of in the following months, allowing a smooth, stall-free camera operation.

The beamtime's applicants are grateful for the instrumental developments that have been undertaken by the beamline staff concerning the installation, preliminary test and first use of this camera on the setup. Additionally, they laud the design and successful use of a novel sample holder allowing for two azimuthal positions and continuous tilt while fitting into the electromagnet's 15-mm gap, thus allowing to use all of the available range of magnetic fields during experiments. The obtained tomographic image series and implementations regarding magnetic fields testify to the fruitful collaboration between the beamline staff and the group of applicants.

In terms of experimental results, we have first shown that the image quality in XMCD-FTH on ID32 can be on par with that of the SEXTANTS beamline at SOLEIL (with sample Beutier17); in particular, we have determined working conditions yielding a much better coherence on ID32 while retaining sufficient flux for imaging. Then, we took advantage of the setup's electromagnet to perform a check on the NiFe teardrop sample that was not possible on SEXTANTS; unfortunately, this sample did not prove suitable for the magnetic vector imaging. Finally, we have performed two series of FTH imaging on the Dann112 Fe/Gd multilayer, aiming at the announced vector tomographic reconstruction. Taking the numerous detector-related problems, we strived to measure at a larger number of angles rather than obtaining large statistics on a few sample tilts so as to prove the feasibility of the technique. The final steps of combining our acquired images in order to obtain a three-dimensional, vectorial reconstruction of magnetization are still ongoing at the time of writing.

References

- [1] Geilhufe *et al.*, *Ultramicroscopy* **214**, 113005 (2020)
- [2] Eisebitt *et al.*, *Nature* **432**, pp. 885-888 (2004)
- [3] Tieg *et al.*, *Optics Express* **26**, 27251 (2010)
- [4] Duckworth *et al.*, *New Journal of Physics* **15**, 023045 (2013)
- [5] Guizar-Sicairos and Fienup, *Optics Express* **15**, 17592 (2007)
- [6] Blanco-Roldán *et al.*, *Nature Communications* **6**, 8196 (2015)
- [7] Streubel *et al.*, *Nature Communications* **6**, 7612 (2015)
- [8] Donnelly *et al.*, *Physical Review B* **94**, 064421 (2016)
- [9] Witte *et al.*, *Nano Letters* **20**, pp. 1305-1314 (2020)
- [10] Desjardins *et al.*, *Journal of Synchrotron Radiation* **27**, pp. 1577-1589 (2020)
- [11] Heald and Stern, *Physical Review B* **16**, 5549 (1977)